Conductivity of an atomically defined metallic interface

David J. Oliver[a,1], **Jesse Maassen**[a,b], **Mehdi El Ouali**[a], **William Paul**[a], **Till Hagedorn**[a], **Yoichi Miyahara**[a], **Yue Qi**[c], **Hong Guo**[a], **and Peter Grütter**[a]

[a]Department of Physics, McGill University, Montreal, QC, Canada H3A2T8; [b]Network for Computational Nanotechnology, Purdue University, West Lafayette, IN 47907; and [c]Chemical and Materials Systems Lab, General Motors R&D Center, Warren, MI, 48090

Edited by William D. Nix, Stanford University, Stanford, CA, and approved September 26, 2012 (received for review May 28, 2012)

A mechanically formed electrical nanocontact between gold and tungsten is a prototypical junction between metals with dissimilar electronic structure. Through atomically characterized nanoindentation experiments and first-principles quantum transport calculations, we find that the ballistic conduction across this intermetallic interface is drastically reduced because of the fundamental mismatch between s wave-like modes of electron conduction in the gold and d wave-like modes in the tungsten. The mechanical formation of the junction introduces defects and disorder, which act as an additional source of conduction losses and increase junction resistance by up to an order of magnitude. These findings apply to nanoelectronics and semiconductor device design. The technique that we use is very broadly applicable to molecular electronics, nanoscale contact mechanics, and scanning tunneling microscopy.

atomic force microscopy | surface science

A key challenge in all nanoscale electrical measurements, including transport measurements on molecules (1) and nanomaterials (2) and quantum break–junction experiments (3), is to accurately determine the area over which contact is made. This determination becomes very difficult at scales of tens of nanometers or less. This challenge is currently a major hindrance in molecular electronics, where poorly defined contact geometries prohibit quantitative testing and refinement of theoretical models against experimental data (2). Junction area is often inferred from conductance in metallic break–junction experiments (for instance, from the Sharvin model) (3), but this approach prevents any conclusions to be made about the relationship between conductance and area. Moreover, it requires a simple, fixed relationship between area and conductance, which we experimentally show below cannot always be assumed. We address this challenge by using a technique that independently and accurately determines the geometry of the tip making contact.

As conducting wires are scaled down in electronic devices, maintaining a low resistance becomes increasingly problematic, with interfaces dominating the total resistance (4). Line widths of wire interconnects on semiconductor chips are forecasted to fall below 16 nm over the next decade (5). Because these length scales are less than the mean free path of electrons (~40 nm for gold), ballistic effects become important. To quantify the resistivity of nanoscale metallic interfaces, precise knowledge of the contact area is needed as well as an understanding of effects such as plastic deformation and tip–substrate interface, which may influence the conductance.

As a first step to achieving an accurate knowledge of contact geometry, we use field ion microscopy (FIM) to image the indenter tip, a microscopy technique that is historically notable for being the earliest technique to directly image individual atoms in real space (6, 7). This capacity is incorporated into a scanning probe arrangement operating in ultra-high vacuum (UHV) capable of simultaneously measuring current and force. FIM is used to characterize the tungsten probe tip with atomic precision. The tip used in this study terminates with a spherical apex having a radius of 4.1 nm (Fig. 1). Nanoindentation experiments were performed, in which the tip is pushed into the surface and retracted, continuously measuring force between the tip and sample as well as relative displacement between the tip and sample. The tungsten tip was used to nanoindent clean Au(111) surfaces to form an electrical junction, with contact dimensions ranging from a few to 50–60 nm^2.

Results

The force–displacement curve obtained from nanoindentation allows plastic deformation in the gold to be observed in the form of displacement bursts as well as overall hysteresis between the loading and unloading curves (Fig. 2*A*). Plastic deformation results in a permanent impression after unloading (Fig. 2*B*). For a probe of this size, loads of 200 nN and above are sufficient to induce permanent plastic deformation, which is determined by the onset of hysteresis (*SI Text*, Figs. S1 and S2). The force–displacement response was analyzed using the Oliver–Pharr method (*Methods*) (8) combined with the measured contact geometry of the tip (Fig. 1) to obtain the hardness, a measure of the contact pressures required to generate plastic deformation in the gold. Strikingly high hardness values were observed (Fig. 2*C*), ranging from 10 to 15 GPa. These values exceed the hardness values obtained in macroscopic tests from gold, a metal known and valued for millenia for its soft malleability (9), by more than an order of magnitude (10). For comparison, the values measured here are similar to the macroscopic hardness of quartz (11). This finding is an instance of the well-documented size effect, where plastic deformation is constrained when the stressed volume is small, dramatically increasing the hardness (10, 12–19). The slight increase of hardness with increasing force in Fig. 2*C* could be attributable to work hardening, whereby preexisting defects impede additional defect propagation (20).

With the hardness, we can determine the contact area and attempt to understand conductance. Electronic conductance through a microscopic metallic constriction has been extensively studied as a means to understand ballistic electron transport (21–24). In the simplest picture, the Sharvin model (3), conductance is simply proportional to the number of ballistic conduction channels across the restriction, equivalent in this case to the contact area. At first glance, this picture is qualitatively consistent with the data: the conductance increases with increasing force/contact area (Fig. 2*A*). However, the maximum conductance in Fig. 2*A* is ~25 G_0, where $G_0 \sim 7.75 \times 10^{-5}\ \Omega^{-1}$ is the conductance quantum which is far lower than the expected conductance based on a simple Sharvin model. From the maximum force of 340 nN and a hardness of 10 GPa obtained using the FIM-reconstructed tip, a contact area can be calculated of 34 nm^2 or ~470 gold atoms. If each atom contributed a full conduction channel, a Sharvin conductance of 470 G_0 would be obtained. Maximum conductance is plotted vs. maximum force for all indents in Fig. 3*A*, and in all cases, conductance

---

Author contributions: J.M., M.E.O., T.H., Y.M., Y.Q., H.G., and P.G. designed research; D.J.O., J.M., M.E.O., W.P., and T.H. performed research; Y.Q. contributed new reagents/analytic tools; D.J.O. and J.M. analyzed data; and D.J.O. and J.M. wrote the paper.

The authors declare no conflict of interest.

This article is a PNAS Direct Submission.

[1]To whom correspondence should be addressed. E-mail: oliverd@physics.mcgill.ca.

This article contains supporting information online at www.pnas.org/lookup/suppl/doi:10.1073/pnas.1208699109/-/DCSupplemental.

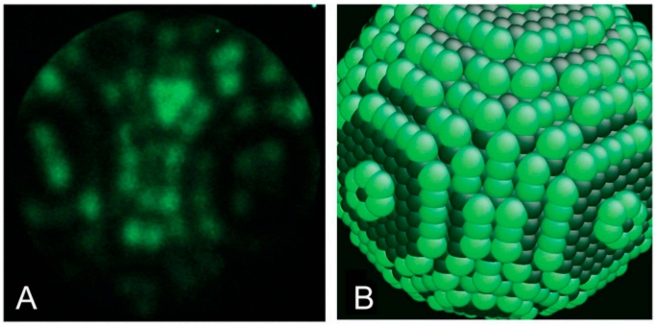

Fig. 1. (*A*) Atomic-resolution FIM image of the W tip used in this study. (*B*) Reconstruction of the tip using a spherical geometry of radius 4.1 nm. Atom sites with high local curvature, visible in FIM, are highlighted bright green.

is much lower than a model based on full ballistic contribution would predict. Additionally, the conductance is typically not constant over repeated unloading and reloading cycles in the same location (Fig. 3*A* and *SI Text*, Figs. S3 and S4). A wide variance of conductance is observed for indentations to the same load and thus, approximately the same contact area, although with an apparent upper bound (Fig. 3*A*). (We note that much less variance is observed in the maximum indentation depth, which is implicit in the consistency of the hardness values in Fig. 2*C*.) Thus, the data are not adequately explained by a simple Sharvin model (3).

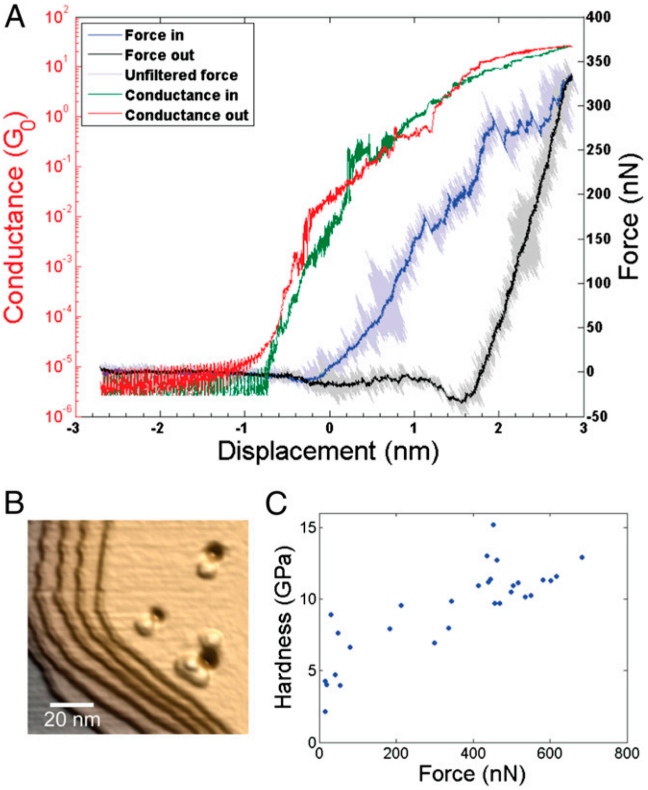

Fig. 2. (*A*) Typical force–displacement (blue and black) and current–displacement (green and red) curves for indentation into (111) gold in UHV using the 4.1-nm W tip shown in Fig. 1. Tunneling current is observed before the onset of adhesive force. (*B*) Scanning tunneling microscopy constant-current topographic image showing permanent deformation after indentation. The steps visible, as well as the pile-up features adjacent to indents, are monatomic Au(111) steps of height 2.4 Å. (*C*) Hardness (maximum contact pressure) values from 30 indents into pristine gold.

We identify two important factors likely to cause deviation from ideal ballistic transport, and both are illustrated in Fig. 3*C*. One possible factor is the W–Au interface. The other factor is the presence of defects within the gold generated by plastic deformation. Molecular dynamics (MD) simulations were carried out of indentation of W into Au: the size scale of the experiment is sufficiently small that a one-to-one spatial mapping with simulation is possible using the atomic structure of the W tip obtained from FIM (Fig. 1*B*). In the MD, indentation was found to generate numerous dislocations beneath the contact area. Fig. 3*B* shows stacking fault ribbons on the close packed (111) planes [indicated by the blue atoms that have centrosymmetry (16) parameters ∼ 0.3] sandwiched between two [112]/6 partials that form a total Burgers vector of [110]/2. Based on the orientations of the stacking faults generated, the conduction path of electrons also has to pass dislocations and stacking fault planes, which is illustrated schematically in Fig. 3*C*. A maximum contact pressure of ∼6 GPa at loads up to 300 nN was found from the MD, reasonably comparable with the experimentally measured hardness. The effect of these two factors, the W–Au interface and the defective Au region, was evaluated with the aid of state-of-the-art quantum transport calculations.

To predict the transport properties of an interface formed from dissimilar materials with different electronic properties, with Au being primarily an s-type metal and W being a d-type metal, first-principles transport calculations were performed. The simulated W(111)/Au(111) interface is shown in Fig. 4 *A* and *B*, where electronic transport is oriented perpendicular to the interface (*z* direction). The atomic structure of the interface was formed by matching the face-centred cubic (FCC) lattice of Au to the body-centred cubic (BCC) lattice of W and allowing the atoms to relax to their equilibrium positions. Pure Au and pure W were also simulated.

Results are shown in Fig. 4. The total conductance per unit area is similar for both metals: $g_{\mathrm{W}} = 8.7\ \mathrm{G_0/nm^2}$ for W and $g_{\mathrm{Au}} = 10.5\ \mathrm{G_0/nm^2}$ for Au. However, by joining the two highly conducting metals, one finds a conductance density of $g_{\mathrm{W/Au}} = 2.8\ \mathrm{G_0/nm^2}$, which is dramatically lower (∼4×) than the conductance density of either material individually.

This surprisingly high interface resistance cannot be explained by low transmission overlap in **k**-space. Fig. 4 *C* and *E* shows the transmission plotted in reciprocal space [$T_{\mathbf{k}}$, where $\mathbf{k} = (k_x, k_y)$] for pure W(111) and pure Au(111), respectively. The $T_{\mathbf{k}}$ distributions reflect the shape of the Fermi surface projected on the *x*–*y* plane. However, complicated $T_{\mathbf{k}}$ patterns arise, because the simulation box is much larger than the unit cells of W and Au. In the absence of scattering, each **k**-point is independent and for pure materials, provides an integer number of quantum channels that each contribute a conductance $\mathrm{G_0}$ (Fig. 4 *C* and *E*). The average conductance of the $T_{\mathbf{k}}$ distribution equals the total conductance per unit area given above. When joining two different materials, the maximum possible ballistic conductance without scattering corresponds to the transmission value at each **k** of the more resistive material. Thus, the regions of high transmission in **k**-space, for both W and Au, must overlap for the total transmission across the interface to remain elevated. By calculating the overlap from Fig. 4 *C* and *E*, we find a maximum possible conductance per unit area of $8.5\mathrm{G_0/nm^2}$, which is nearly identical to g_{W}. This finding indicates that the high-interface resistance of $g_{\mathrm{W/Au}} = 2.8\ \mathrm{G_0/nm^2}$ is not because of poor **k**-space overlap. Moreover, an analysis of the atomic structure confirms that the interfacial atoms possess a similar number of nearest neighbors as in their bulk form; hence, there are no voids that could decrease conductance. We conclude that the reduction in conductance derives from the orbital mismatch between W and Au, which increases the probability of backscattering at the interface.

The theoretically calculated W–Au conductance density, combined with the contact area of the W–Au junction, can be used to obtain a relation between conductance and force (Eq. **1**):

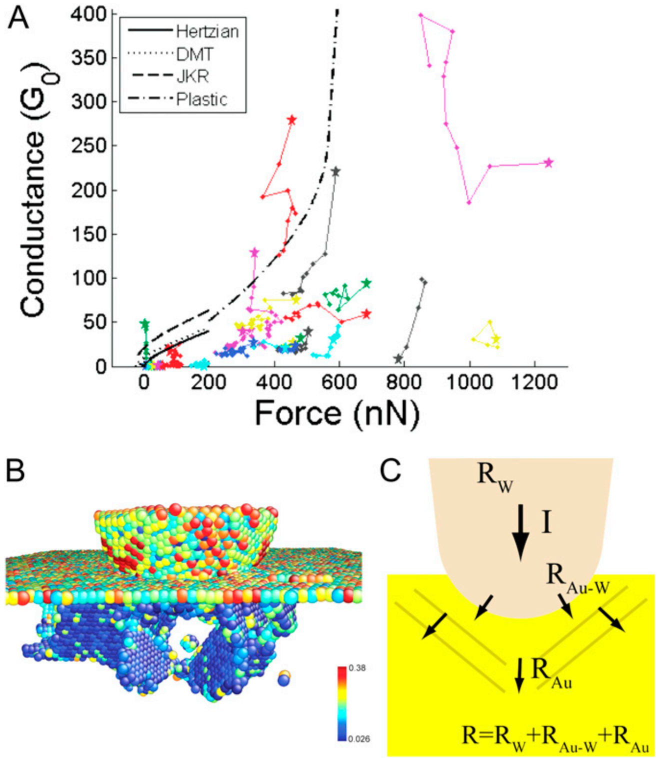

Fig. 3. (*A*) Evolution of conductance with repeated indentation. Each point represents a single indentation; each linked set of points is a sequence of indentations in the same location. (The starred point is the first indentation in the sequence.) Black curves are calculated upper bounds on the conductance (Eq. **1**), assuming that the W–Au interface is the only source of resistance in the junction, obtained by multiplying the interface resistance given by quantum transport calculations by the contact area given by elastic (Hertzian, DMT, and JKR) and plastic models. (*B*) Snapshot of an MD simulation showing dislocations and planar defects generated in gold by plastic deformation. Atoms are colored by centrosymmetry parameter (16); only atoms deviating from bulk symmetry are visible. (*C*) Schematic illustrating the conduction path through the W–Au junction and associated resistance sources: the W–Au interface itself and the defective Au region.

$$G = gA(F) = 2.8\ \mathrm{G_0/nm^2}\,A(F), \qquad [1]$$

where G is total conductance, g is calculated conductance density, A is contact area, and F is force. Contact area can be derived in the high-load, plasticity-dominated regime directly from the experimentally determined hardness ($H \sim 10$ GPa) using the relationship $H = F/A$. In the low-load elastic regime, contact area was calculated from several elastic models using the geometry of the tip obtained from FIM and the elastic properties of the two materials. These curves from Eq. **1** are plotted in black in Fig. 3*A* and correspond closely to the upper limits of the measured data. If these data values are assumed to be indentations for which resistance in the gold is minimal because of, for instance, a fortuitous defect configuration that permits a clear conduction pathway, then a strikingly good agreement between theory and experiment is obtained.

Because of the hardness of W, most defects will be formed in the much softer Au substrate. First-principles transport modeling of dislocations is beyond our current computational capability. Therefore, in an attempt to model the effect of imperfections/defects on the transport properties of the W–Au interface, we have considered (*i*) random atomic deviations around the ideal lattice sites of Au and (*ii*) random vacancies in Au. In Fig. 5*A*, examples of random configurations are shown as a function of the disorder parameter d_M. These structures are obtained by randomizing the coordinates of each atom around its ideal lattice, with a maximum possible displacement of d_M times by the Au–Au nearest neighbor distance (2.87 Å).

The conductance histogram for 10 randomly generated atomic configurations as a function of d_M, ranging from 1% to 25%, is presented in Fig. 5*B*. With increasing d_M, in addition to showing a broader distribution in G, the average conductance $\langle G \rangle$ is found to decrease roughly linearly. At $d_M = 25\%$, which corresponds to very high disorder, the conductance drops by only a factor of two compared with a perfect lattice. The conductance drops, because as the atoms are displaced from their equilibrium positions, they get simultaneously closer and further to their neighboring atoms. A larger distance between Au atoms reduces electronic hopping and leads to additional resistance. We note in passing that, according to the criterion in the work by Lindemann (25), a (dynamic) variation from the equilibrium position greater than ∼10% would imply the melting of the solid. As such, the d_M values shown here are solely intended to present the trend of electrical conductance as a function of interatomic distance rather than necessarily represent a physically realistic structure.

Next, we consider the role of vacancies in Au. Our numerical results indicate that the conductance is more sensitive to vacancies than random atomic displacements: at 10% vacancies, G decreases 2×, whereas a factor of 4× is observed for 30%. Vacancies induce local perturbations in the potential and hence, act as scattering sites for electronic waves. As such, conduction decreases because of backscattering, and at higher vacancy percentage (>10%) (*SI Text*, Fig. S5), the lack of atoms begins to inhibit any possible conduction pathway.

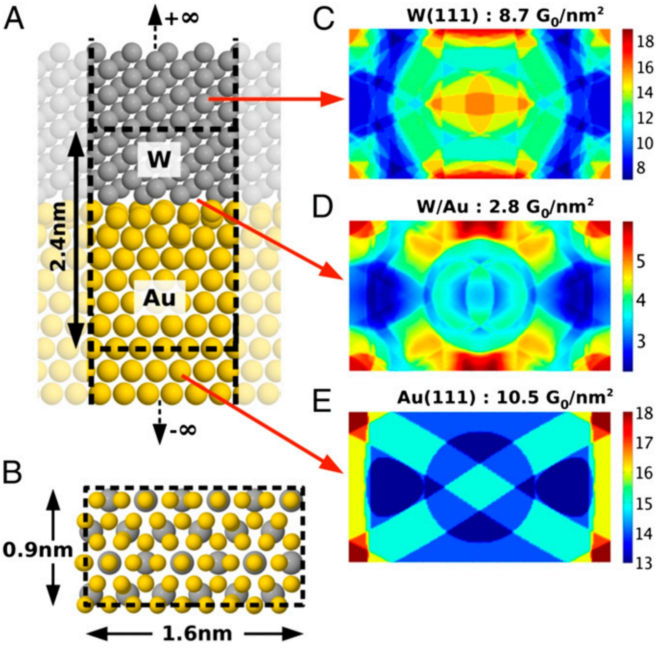

Fig. 4. (*A*) Side view and (*B*) cross-section of the atomic structure of the W(111)–Au(111) interface. The dashed black lines and associated measurements delimit the simulation box for the *ab initio* transport calculations. Both metals are semiinfinite, meaning that the W (Au) extends to +∞ (−∞) along the transport direction; periodic boundary conditions are applied in the plane perpendicular to transport. *C–E* present the transmission coefficient in reciprocal space for pure W(111), the W(111)–Au(111) interface, and pure Au(111), respectively. The total conductance per unit area is also shown.

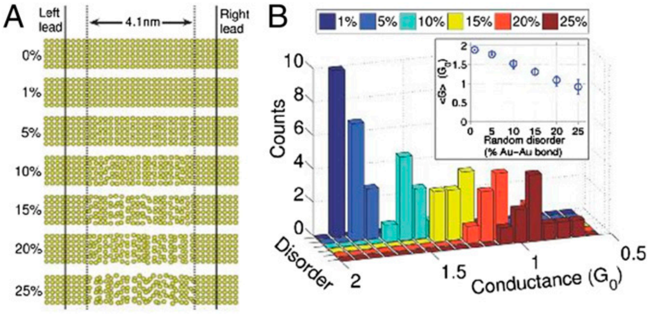

Fig. 5. (*A*) Examples of randomly disordered Au structures as a function of the maximum possible displacement d_M (given in terms of the Au–Au bond length of 2.87 Å) around the perfect lattice site. Transmission is in the [100] direction. (*B*) Conductance histogram for 10 randomly generated Au structures as a function of disorder parameter $d_M = 1\%, 5\%, 10\%, 15\%, 20\%$, and 25%. *B Inset* shows the average conductance as a function of d_M. Note that the conductance values correspond to a cross-sectional area of 0.406 × 0.406 nm. The histograms shown in *B* are plotted separately in Fig. S9.

Discussion

Conductance through the W–Au junction is affected by the intermetallic interface, defects in the Au, and likely, additional factors that we have not considered here, such as departures from interface ideality or adsorbed gas impurities. We summarize the contributions that have been theoretically evaluated in Table 1. The defect contribution is difficult to exactly quantify, because it is presently unfeasible to perform full quantum transport calculations on defect configurations of realistic complexity, configurations with tens or hundreds of thousands of atoms similar to those configurations shown in Fig. 3*B*. Ballistic transmission has been found to be reduced by planar defects, such as twin and grain boundaries (26), in addition to the generalized disorder and point defects modeled here. The process of defect production under indentation stresses has an inherently stochastic element: defects are produced in a pristine crystal by thermally activated nucleation within a limited volume beneath the tip where stresses are highest. The energy landscape for subsequent defect nucleation and propagation will be strongly affected by the presence of the first defect. Macroscopically identical conditions may thereby produce microscopically distinct defect configurations from indent to indent. This result is observed in our MD simulations, where the changing in the initial random seed governing thermal noise is sufficient to produce quite distinct defect configurations. Thus, there are likely to be a range of defect configurations across a set of indents, with the resistance varying according to the electron conduction pathway offered. Such variation will be particularly pronounced at these very small scales, and they may account for the high variance that we measure in conductance. This finding also explains the fact that nearly all experimental data points fall below the upper-bound estimation of the conduction.

In general, an ensemble average of measurements may exhibit a single, fixed conductance–area relationship, even when single measurements in the ensemble show considerable variability. This approach is often used to analyze break–junction experiments (3). It is not necessarily the case, however, in situations such as the one here, where there may be contributing resistance terms that themselves exhibit an areal dependence, such as the defect contribution.

Although we have an accurate definition of the geometry of the indenting tip from FIM, the contact area during indentation can only be extracted by making assumptions about the contact mechanics taking place. Some of these assumptions are undoubtedly simplistic. The Oliver–Pharr method (8), for instance, does not take into account adhesive effects or material pile up around the indenter, both of which are likely to be present at these size scales and both of which affect the contact area. Additionally, at these near-atomic length scales, mass transport mechanisms not commonly associated with nanoindentation, such as point-defect diffusion, will come into play, particularly for metal surfaces with a high mobility, like Au(111) (27, 28). These mechanisms will act to lower stress and increase the contact area relative to the continuum-mechanical prediction. These assumptions do not alter the conclusions drawn here but will need to be corrected for when highly precise conductance measurements are to be made, and a very accurate measure of contact area is, therefore, needed. Thus, to take full advantage of this technique, new contact models are called for that account for the physical processes occurring at these very small size scales.

Tungsten is a poor conductor in the bulk, with a room temperature resistivity ∼3× the resistivity of copper and ∼2.5× the resistivity of gold (11). Interestingly, the calculations here show that, under ballistic conduction, tungsten and gold are almost equally conductive. It is, instead, the interface between the two dissimilar metals that dominates the total resistance. At present, tungsten is used as a chip-level interconnect in complementary metal-oxide-semiconductor (CMOS) circuits (5, 29) in contact with copper, an FCC metal where conductance is dominated by s-like modes (30). These findings suggest that, as semiconductor devices shrink farther to ballistic scales, counterintuitive interface effects are liable to dominate device resistance, particularly for metals with dissimilar electronic structure.

In conclusion, we find that mechanical response and electronic transport in nanometer-scale tungsten-on-gold contacts formed by nanoindentation exhibit pronounced departures from macroscopic behavior. A very high mechanical hardness of ∼10 GPa is observed, indicating that a size effect is operating. Conductance through the W–Au junction exhibits a distinct upper bound, ∼4× less than would be predicted from a simple Sharvin model. First-principles transport calculations show that this 4× drop closely agrees with the expected resistance from ballistic transmission losses across a perfect W–Au interface. Additional decreases in conductance are observed because of defects in the gold generated by plasticity. By atomically characterizing the W probe tip with field ion microscopy, we are able to extract quantitative parameters from experiment and verify the predictions of theory.

Methods

All experiments were carried out in a custom-built combined FIM-STM-AFM system housed in UHV. (Ref. 31 has a detailed overview of the system, and

Table 1. Summary of factors considered to contribute to reduction of the conductance through a gold–tungsten nanomechanical interface relative to the ideal Sharvin prediction

Sharvin condition (G_0/nm^2)	Transmission			Modified condition (G_0/nm^2)	Experimental conditions (G_0/nm^2)
	Interface	Disorder	Vacancies		
13.8	20%	75%	50%	1.03	0.02–4.9

For the disorder and vacancy contributions, the values were taken from Fig. 5*B* and Fig. S8 for physically plausible upper values of 10% disorder and 10% vacancy concentration. The combined effects give an order of magnitude reduction in conductance. The experimental range of conductance for plastic contacts is also shown.

Fig. S6 shows the schematic.) Samples were made by coating 50-μm-thick flexible quartz cantilevers with 100 nm gold by thermal evaporation. Samples were treated by repeated cycles of ion-beam bombardment and high-temperature annealing in UHV to prepare large 111-oriented terraces before being transferred in vacuum to the measurement chamber. Auger spectroscopy was used to verify that the gold surface was free of contaminants directly after sputtering and annealing. The gold-coated cantilever serves as force transducer during scanning and indentation, and its deflection is measured by optical interferometry. W tips were prepared by electrochemical etching followed by annealing in vacuo (32). FIM imaging was performed by leaking He gas into the measurement chamber and applying a sufficiently high voltage (∼4 kV) to ionize the He atoms, which are then accelerated away from the tip to an imaging screen (33, 34). Voltages above the imaging threshold can be applied to field-desorb W atoms to prepare a well-defined tip. After FIM imaging, the system pressure was allowed to return to normal UHV levels ($<2 \times 10^{-10}$ mbars) before performing measurements. See *SI Text* and Figs. S7 and S8 for further detail on FIM imaging and cleanliness considerations.

STM images were obtained in constant-current mode at a voltage of 50 mV and a setpoint current of 100 pA. All experiments were carried out at room temperature. Indentations were performed in the following manner: the tip was brought into tunneling contact with the sample at the setpoint current; it was then retracted 0.5 nm, approached to a nominated extension of the piezoelectric tube controlling the tip height, and then retracted again to 0.5 nm above the setpoint height, with a duration of 1 s for approach and 1 s for retraction. A constant voltage of 50 mV was maintained throughout indentation. Successive indentations in the same location were performed to the same piezoelectric extension each time. Force was not directly controlled, meaning it could vary somewhat for successive indentations, if the height at which the setpoint current was achieved varied. Nonetheless, although force could not be directly controlled, it was precisely and reliably measured. Indentation sequences were spaced at least 10 nm apart to minimize interaction between indents. Current was measured over ∼9 decades (pA to mA) using a logarithmic preamplifier (35). The reported conductance was corrected for the series resistance of the W tip wire of ∼35 Ω. Current sensitivity was ultimately limited in measurements to ∼40 pA, as visible in Fig. 2*A*, by instrumental electronic and capacitively-coupled mechanical noise.

Hardness and elastic modulus were extracted using the Oliver–Pharr method (8). The tip-sample rigid body displacement was found by subtracting the deflection of the transducing cantilever from the piezoelectric extension. For the analysis, the zero displacement, or point of contact, was determined by the onset of a repulsive force of 7 nN (roughly the noise floor of the experiment). For the area function, a spheroconical tip geometry was used, with a radius of 4.1 nm determined from FIM and a cone full angle of 5° measured by scanning EM.

Several elastic models were used to calculate the contact area in the elastic regime for the envelope curves plotted from Eq. **1** in Fig. 3*A*. The simplest, the Hertzian model (36), assumes no adhesion between the tip and substrate, and it has the functional form $A(F)=\pi\left(\frac{3}{4}FR/E^*\right)^{2/3}$, where A is contact area, F is force, R is tip radius, and E^* is the effective elastic modulus. Because adhesion is evident at these size scales, we also used two models that take adhesion into account. In the Johnson–Kendall–Roberts (JKR) model (37), the contact area is allowed to vary in response to adhesive forces within the contact, with zero force outside the contact. The JKR area function is $A(F)=\pi\left(\frac{3}{4}FR/E^*+\frac{3}{4}\pi wR^2/E^*\left(3+\sqrt{9+6F/\pi wR}\right)\right)^{2/3}$, where w is the work of adhesion for tungsten and gold. In the Derjaguin–Muller–Toporov (DMT) model (37), the contact area is the same as the contact area for the Hertzian model, but adhesive forces are allowed to act outside the contact. The DMT area function is given by $A(F)=\pi\left(\frac{3}{4}FR/E^*+\frac{3}{2}\pi wR^2/E^*\right)^{2/3}$. These cross-sectional contact areas were converted into projected areas for the conductance calculation. The values used were $R = 4.1$ nm obtained from FIM, $E^* = 60$ GPa obtained from the Oliver–Pharr analysis, and a typical metallic adhesion energy (17) of $w = 1\ \mathrm{J{\cdot}m^{-2}}$.

Molecular dynamics simulations were carried out using the Large-scale Atomic/Molecular Massively Parallel Simulator (LAMMPS) code. Atomic interactions were modeled by the embedded atom method (38) using a hybridized potential for Au–W interactions (39). Isothermal dynamics were used with a time constant of 1 fs, with the system held at 300 K using the Nose–Hoover thermostat (40). A 111-oriented gold slab of dimensions 25 × 25 × 11 nm was used that was periodic in the x and y directions and had a fixed boundary layer in the z direction. After an initial relaxation period of 50 ps, displacement-controlled indentation was performed by alternately approaching the tip at $0.01\ \mathrm{nm{\cdot}s^{-1}}$ for 2.5 ps and waiting for 5 ps to allow the system to equilibrate. To calculate pressure from MD configurations, contact area was extracted by dividing the configuration into 1 × 1 × 1-Å voxels, which were tested for atomic occupancy assuming an atomic radius of 1.91 Å. The contact area then corresponded to the x–y voxel area at the z depth of contact between W and Au or equivalently, the minimum x–y voxel area in the configuration.

The modeled W–Au interface was obtained by matching 3× the Au lattice (experimental lattice constant $a_{\mathrm{Au}} = 4.08$ Å) to 4× the W lattice ($a_{\mathrm{W}} = 3.16$ Å) along the (111) plane, leading to a cross-section of $l_x = 15.48$ Å × $l_y = 8.94$ Å. The final atomic structure was calculated by relaxing the coordinates of the atoms by total energy minimization within the VASP package (41, 42), and therefore, the forces were less than 0.02eV/Å per atom. A plane–wave basis energy cutoff of 250 eV, the projector augmented wave method, and the local density approximation for exchange-correlation potential were used. The conductance of the W–Au interface was calculated using the MATDCAL transport simulation package (43) based on the nonequilibrium Green's function–density functional theory (NEGF-DFT) formalism (44). Our linear combination of atomic orbitals basis consisted of *s*-, *p*-, and *d*-orbitals used in conjunction with nonlocal pseudopotentials to represent the nucleus/core. A **k**-mesh of $(k_x, k_y) = (9, 17)$ was used for the self-consistent electronic density, and $(k_x, k_y) = (101, 175)$ was used for the conductance. When simulating the nonideal cases of (*i*) atomic disorder in Au and (*ii*) the presence of random vacancies in Au, we used a cross-section of 4.06 × 4.06 Å; *i* was modeled using MATDCAL [$(k_x, k_y) = (11, 11)$: self-consistent density, $(k_x, k_y) = (101, 101)$: conductance], whereas *ii* simulated random configurations of vacancies within the linear muffin-tin orbital–coherent potential approximation (LMTO-CPA) variant of the NEGF-DFT technique (45) [$(k_x, k_y) = (25, 25)$: self-consistent density, $(k_x, k_y) = (300, 300)$: conductance]. In the case of atomic disorder, the atomic structure of a given simulation was obtained by randomly displacing each atom in the scattering region around its equilibrium lattice position. The maximum magnitude of displacement is set to $d_M \times a_{\mathrm{Au}}/\sqrt{2}$, where d_M is defined as the fraction of the nearest neighbor distance in Au, $a_{\mathrm{Au}}/\sqrt{2}$. To extract the average effect of random atomic disorder, for each value of d_M, we generate 10 separate random atomic configurations, calculate the conductance of each configuration, and finally, compute the average conductance.

ACKNOWLEDGMENTS. Funding for this research was provided by the Natural Sciences and Engineering Research Council of Canada, le Fonds Québécois de le Recherche sur la Nature et les Technologies, and the Canadian Institute for Advanced Research.

1. Moth-Poulsen K, Bjørnholm T (2009) Molecular electronics with single molecules in solid-state devices. *Nat Nanotechnol* 4(9):551–556.
2. Léonard F, Talin AA (2011) Electrical contacts to one- and two-dimensional nanomaterials. *Nat Nanotechnol* 6(12):773–783.
3. Agrâit N, Yeyati AL, van Ruitenbeek JM (2003) Quantum properties of atomic-sized conductors. *Phys Rep* 377:81–279.
4. Pop E (2010) Energy dissipation and transport in nanoscale devices. *Nano Res* 3: 147–169.
5. Interconnect (2009) *International Technology Roadmap for Semiconductors* (Interconnect). Available at http://www.itrs.net/Links/2009ITRS/Home2009.htm.
6. Müller EW, Bahadur K (1956) Field ionization of gases at a metal surface and the resolution of the field ion microscope. *Phys Rev* 102:624–631.
7. Melmed AJ (2002) Erwin Müller—memoir. *Biogr Mem Natl Acad Sci*, 82. Available at http://www.nap.edu/readingroom.php?book=biomems&page=emueller.html.
8. Oliver WC, Pharr GM (1992) An improved technique for determining hardness and elastic modulus using load and displacement sensing indentation experiments. *J Mater Res* 7:1564–1583.
9. Pliny (1855) *Natural History*. trans Bostock J, Riley HT (H. G. Bohn, London), Vol 6, pp 96–98.
10. Nix WD, Greer JR, Feng G, Lilleodden ET (2007) Deformation at the nanometer and micrometer length scales: Effects of strain gradients and dislocation starvation. *Thin Solid Films* 515:3152–3157.
11. CRC (2011) *CRC Handbook of Chemistry and Physics, 92nd Ed., Handbook of Chemistry and Physics* (CRC, Boca Raton, FL), pp 12–225.
12. Sutton AP, Pethica JB (1990) Inelastic flow processes in nanometre volumes of solids. *J Phys Condens Matter* 2:5317.
13. Landman U, Luedtke WD, Burnham NA, Colton RJ (1990) Atomistic mechanisms and dynamics of adhesion, nanoindentation, and fracture. *Science* 248(4954):454–461.
14. Corcoran SG, Colton RJ, Lilleodden ET, Gerberich WW (1997) Anomalous plastic deformation at surfaces: Nanoindentation of gold single crystals. *Phys Rev B* 55:R16057.
15. Kiely JD, Houston JE (1998) Nanomechanical properties of Au (111), (001), and (110) surfaces. *Phys Rev B* 57:12588.
16. Kelchner CL, Plimpton SJ, Hamilton JC (1998) Dislocation nucleation and defect structure during surface indentation. *Phys Rev B* 58:11085.

17. Cross GLW, Schirmeisen A, Grütter P, Dürig UT (2006) Plasticity, healing and shakedown in sharp-asperity nanoindentation. *Nat Mater* 5(5):370–376.
18. Navarro V, de la Fuente OR, Mascaraque A, Rojo JM (2008) Uncommon dislocation processes at the incipient plasticity of stepped gold surfaces. *Phys Rev Lett* 100(10):105504.
19. Ward DK, et al. (2009) Engineering size-scaling of plastic deformation in nanoscale asperities. *Proc Natl Acad Sci USA* 106(24):9580–9585.
20. Courtney TH (2000) *Mechanical Behavior of Materials* (McGraw-Hill, New York), 2nd Ed.
21. Marszalek PE, Greenleaf WJ, Li H, Oberhauser AF, Fernandez JM (2000) Atomic force microscopy captures quantized plastic deformation in gold nanowires. *Proc Natl Acad Sci USA* 97(12):6282–6286.
22. Rubio-Bollinger G, Bahn SR, Agraït N, Jacobsen KW, Vieira S (2001) Mechanical properties and formation mechanisms of a wire of single gold atoms. *Phys Rev Lett* 87:026101.
23. Kizuka T (2008) Atomic configuration and mechanical and electrical properties of stable gold wires of single-atom width. *Phys Rev B* 77:155401.
24. Armstrong JN, Hua SZ, Chopra HD (2011) Mechanics of quantum and Sharvin conductors. *Phys Rev B* 83:235422.
25. Lindemann FA (1910) The calculation of molecular vibration frequencies. *Z Phys* 11:609.
26. Feldman B, Park S, Haverty M, Shankar S, Dunham ST (2010) Simulation of grain boundary effects on electronic transport in metals, and detailed causes of scattering. *Phys Stat Sol B* 247:1791–1796.
27. Emch R, Nogami J, Dovek MM, Lang CA, Quate CF (1989) Characterization of gold surfaces for use as substrates in scanning tunneling microscopy studies. *J Appl Phys* 65:79–84.
28. Lauer ME, et al. (2007) Formation and healing of micrometer-sized channel networks on highly mobile Au(111) surfaces. *Langmuir* 23(10):5459–5465.
29. Havemann RH, Hutchby JA (2001) High-performance interconnects: An integration overview. *Proc IEEE* 89:586–601.
30. Ashcroft NW, Mermin ND (1976) *Solid State Physics* (Holt, Rinehart and Winston, New York).
31. El Ouali M (2010) Nanometre scale indentation: Effect of very sharp indenters on adhesion, plasticity, and electronic transport. PhD thesis (McGill University, Montreal).
32. Hagedorn T, et al. (2011) Refined tip preparation by electrochemical etching and ultrahigh vacuum treatment to obtain atomically sharp tips for scanning tunneling microscope and atomic force microscope. *Rev Sci Instrum* 82(11):113903–113905.
33. Tsong TT (1990) *Atom-Probe Field Ion Microscopy* (Cambridge Univ Press, Cambridge UK).
34. Lucier A-S, Mortensen H, Sun Y, Grutter P (2005) Determination of the atomic structure of scanning probe microscopy tungsten tips by field ion microscopy. *Phys Rev B* 72:235420.
35. Dürig U, Novotny L, Michel B, Stalder A (1997) Logarithmic current-to-voltage converter for local probe microscopy. *Rev Sci Instrum* 68:3814–3816.
36. Johnson K (1985) *Contact Mechanics* (Cambridge Univ Press, Cambridge, UK).
37. Maugis D (1999) *Contact, Adhesion, and Rupture of Elastic Solids* (Springer, Berlin).
38. Daw MS, Foiles SM, Baskes MI (1993) The embedded-atom method: A review of theory and applications. *Mater Sci Rep* 9:251–310.
39. Zhou XW, Johnson RA, Wadley HNG (2004) Misfit-energy-increasing dislocations in vapor-deposited CoFe/NiFe multilayers. *Phys Rev B* 69:144113.
40. Hoover WG (1985) Canonical dynamics: Equilibrium phase-space distributions. *Phys Rev A* 31(3):1695–1697.
41. Kresse G, Furthmüller J (1996) Efficient iterative schemes for *ab initio* total-energy calculations using a plane-wave basis set. *Phys Rev B* 54(16):11169–11186.
42. Kresse G, Furthmüller J (1996) Efficiency of ab-initio total energy calculations for metals and semiconductors using a plane-wave basis set. *Comput Mater Sci* 6:15.
43. Waldron D, Haney P, Larade B, MacDonald A, Guo H (2006) Nonlinear spin current and magnetoresistance of molecular tunnel junctions. *Phys Rev Lett* 96(16):166804.
44. Taylor J, Guo H, Wang J (2001) *Ab initio* modeling of quantum transport properties of molecular electronic devices. *Phys Rev B* 63:245407.
45. Ke Y, Xia K, Guo H (2008) Disorder scattering in magnetic tunnel junctions: Theory of nonequilibrium vertex correction. *Phys Rev Lett* 100(16):166805.